Materials Research Letters

ISSN: (Print) 2166-3831 (Online) Journal homepage: https://www.tandfonline.com/loi/tmrl20

Deformation-free geometric recrystallisation in a metastable β-Ti alloy produced by selective laser melting

Ahmad Zafari, Edward W. Lui & Kenong Xia

To cite this article: Ahmad Zafari, Edward W. Lui & Kenong Xia (2020) Deformation-free geometric recrystallisation in a metastable β-Ti alloy produced by selective laser melting, Materials Research Letters, 8:3, 117-122, DOI: 10.1080/21663831.2020.1713244

To link to this article: https://doi.org/10.1080/21663831.2020.1713244

MATER. RES. LETT.
2020, VOL. 8, NO. 3, 117–122
https://doi.org/10.1080/21663831.2020.1713244

MATERIALS RESEARCH LETTERS
Taylor & Francis
Taylor & Francis Group

ORIGINAL REPORT

Deformation-free geometric recrystallisation in a metastable β-Ti alloy produced by selective laser melting

Ahmad Zafari [a], Edward W. Lui [a,b] and Kenong Xia [a]

[a]Department of Mechanical Engineering, University of Melbourne, Melbourne, Australia; [b]Centre for Additive Manufacturing, School of Engineering, RMIT University, Melbourne, Australia

ABSTRACT

Super-transus heat treatments conducted on an additively manufactured body-centred-cubic β-Ti alloy led to the formation of equiaxed β grains from an initially columnar structure. The grain structure was transformed thanks to a combination of Plateau-Rayleigh instability and grain growth driven by reduction in grain boundary surface area. This is a new type of geometric recrystallisation with no deformation involved. Other mechanisms proposed based on either deformation-induced recrystallisation or martensitic decomposition are dismissed owing to low dislocation density and absence of martensitic transformation in the alloy studied.

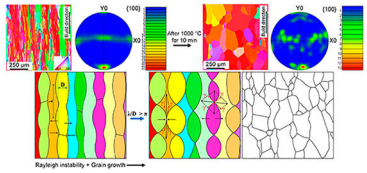

IMPACT STATEMENT

Columnar to equiaxed transformation of β by super-tranus heat treatment of SLM-fabricated Ti is due to Rayleigh instability and grain growth, dismissing the belief that usual deformation-driven recrystallisation is responsible.

ARTICLE HISTORY
Received 24 September 2019

KEYWORDS
Titanium alloys; equiaxed microstructure; grain growth; recrystallisation; selective laser melting

1. Introduction

The epitaxial growth of crystals during additive manufacturing (AM) of Ti creates columns of bcc-structured prior β grains along $< 100 >$ [1,2], leading to a significant anisotropy in mechanical properties [3–5]. It is desirable to replace the as-AM grain structure by an equiaxed one, achievable by heat treatment (HT) above the β transus temperature (T_β) [6] or deposition on a pre-heated substrate using proper parameters, as in the case of electron beam melting (EBM) [7]. This morphological change was first observed in an SLM-fabricated α-β Ti–6Al–4V heat treated at 1200°C for 5 min [6]. No mechanism was suggested, although recrystallisation was ruled out since the equiaxed grains obtained were larger than those after recrystallisation in the counterpart wrought alloys. On the other hand, the transformation into equiaxed grains during wire and arc AM of Ti–6Al–4V [8] was attributed to recrystallisation, based on the argument that the ultra-high cooling rates induced large thermal stresses leading to increased dislocation density high enough to cause recrystallisation, although no evidence was provided. A recent study [9] on Ti–6Al–4V by EBM plus hot isostatic pressing (HIP) at super-transus temperatures proposed that decomposition of martensitic α' during EBM created β grains with different orientations from that of the prior β and they grew during HIP to produce randomly oriented, equiaxed grains. These studies, however, hypothetically proposed mechanisms based on the final microstructure after HTs without investigating the early stages of the transformation. Further, they all focused on the α-β Ti–6Al–4V alloy which experienced martensitic transformation, raising the question whether equiaxed

CONTACT Ahmad Zafari zafari.a@unimelb.edu.au Department of Mechanical Engineering, University of Melbourne, Parkville, VIC 3010, Australia; Kenong Xia k.xia@unimelb.edu.au Department of Mechanical Engineering, University of Melbourne, Parkville, VIC 3010, Australia

Supplemental data for this article can be accessed here. https://doi.org/10.1080/21663831.2020.1713244

β grains can also form in additively manufactured β-Ti alloys with no martensitic transformation upon quenching, and if so, what mechanism is responsible.

To close this gap, here we produced a β Ti–5Al–5V–5Mo–3Cr–0.5Fe (Ti-5553) using selective laser melting (SLM), and performed HTs at super-transus temperatures for short times to observe early stages of the morphological transformation. Equiaxed β formed without involving martensite decomposition or dislocation-based recrystallisation. Instead, the high surface area of β columns was the driving force. A new mechanism was proposed based on Plateau-Rayleigh instability and grain growth driven by reduction in the grain boundary area.

2. Experimental materials and procedures

A plasma atomised Ti–5Al–5V–5Mo–3Cr–0.5 Fe (wt.%) powder (15−45 µm) supplied by AP&C was used (the chemical composition in Table S1 in the Supplementary Materials). Renishaw AM250 was employed for printing rods of ϕ 8×20 mm using stripe scanning strategy on a titanium substrate at room temperature in an atmosphere containing $<<$ 100 ppm oxygen. Other printing parameters are listed in Table 1. Density of 99.7% relative to 4.65 g/cm^3 for Ti-5553 [10] was achieved. Heat treatments were conducted at 1000°C ($>$ T$_\beta$ of $\sim$845°C [11]) for 0.5–10 min followed by iced-water quenching.

Microstructures were characterised by SEM (FEI Quanta FEG200 and Teneo Volume Scope), and TEM (FEI Tecnai F20). TEM samples were cut using focused ion beam (FEI Nova 200 Nanolab DualBeam). AZtec HKL Standard with Symmetry 51N2033 was employed to acquire EBSD maps using 20 kV, 9.5 nA and step sizes of 1–5 µm. When needed, samples were etched using Kroll's Reagent.

3. Results

Figure 1(a) shows EBSD IPF-Y map of as-SLM Ti-5553, revealing β columns of $\sim$10–40 µm in width and

Table 1. Main printing parameters used.

Stripe size (mm)	Layer thickness (µm)	Point distance (µm)	Exposure time (µs)	Power (W)	Hatch spacing (mm)	Laser spot size (µm)	Rotation angle between layers (°)
5	30	55	70	200	0.105	66	67

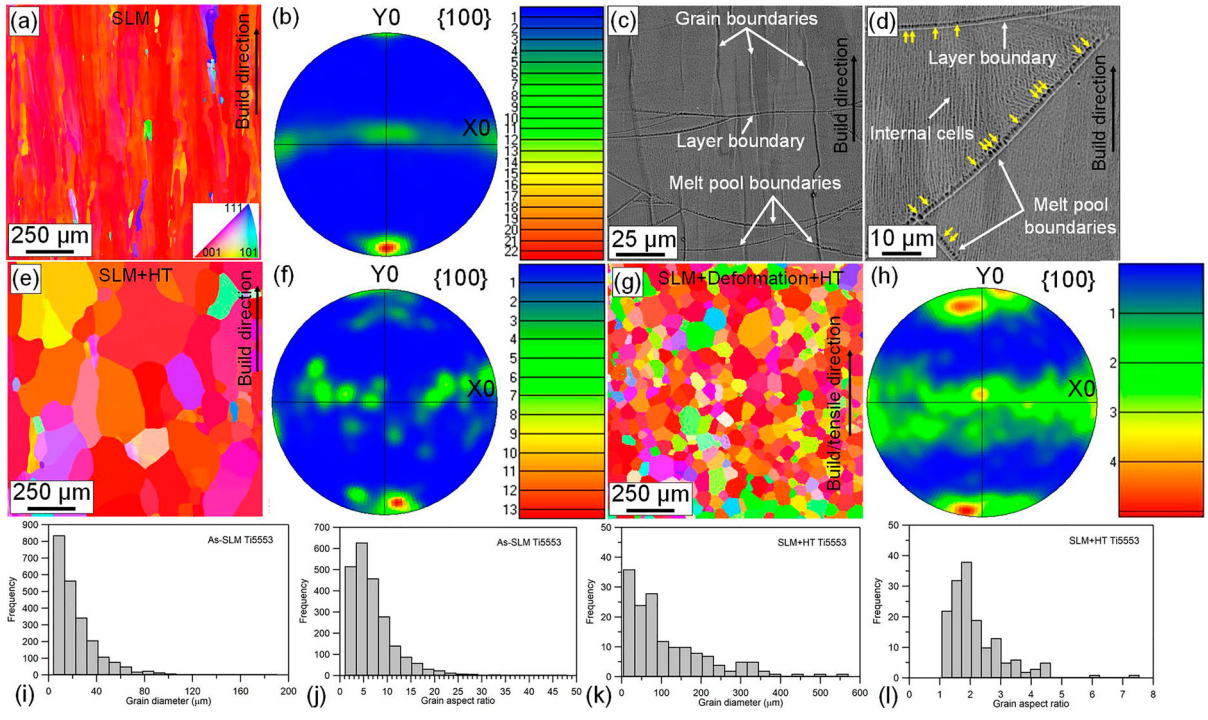

Figure 1. (a,b) EBSD of the as-SLM Ti-5553, showing (a) IPF map with respect to axis-Y (IPF-Y) parallel to the build direction and (b) {100} pole figure, revealing β grains with preferred orientation of $<$ 100 $>$. (c,d) SEM of the as-SLM Ti-5553, showing grain boundaries, melt pool and layer boundaries, internal cells of $<$ 1 µm in thickness, and etch pits (arrowed) in the melt pool and layer boundaries. (e,f) EBSD of the SLM Ti-5553 after HT at 1000°C for 10 min, showing (e) IPF-Y and (f) {100} pole figure, revealing the same texture as that in (b) with slightly lower intensity. (g,h) EBSD from the necking area of SLM Ti-5553 subjected to tensile testing along the build direction followed by HT at 1000°C for 10 min, showing (g) IPF-Y and (h) {100} pole figure, revealing significantly weakened texture. (i,j) The distributions of β grain sizes and aspect ratios, respectively, in the as-SLM Ti-5553 and (k,l) those after HT for 10 min.

$\sim$400–500 µm in length. The grain boundary density (ρ_{GB}) in Figure 1(a) was estimated to be 95 mm/mm^2. {100} pole figure in Figure 1(b) indicates that $<100>$ with the intensity of $\sim$22 multiples of uniform distribution (MUD) are aligned with build and crystal growth directions (complete sets of data for all alloys in Supplementary Material). SEM showed straight grain boundaries and melt pool and layer boundaries (Figure 1(c)). A closeup in Figure 1(d) reveals internal cells of <1 µm thick, and etch pits (yellow arrows) in the melt pool and layer boundaries, later identified as dislocations using TEM.

Figure 1(e–f) shows the EBSD IPF-Y map and {100} pole figure, respectively, of the SLM Ti-5553 after HT at 1000°C for 10 min. The morphology of β grains was changed into equiaxed with ρ_{GB} of 12 mm/mm^2, 8 times smaller than that before HT. However, the {100} pole figure (Figure 1(f)) revealed that the general texture remained the same as that before HT (i.e. $<100>$ were mostly oriented along the build direction) although its intensity ($\sim$14 MUD) was lower. For comparison, EBSD was conducted on SLM Ti-5553 after tensile deformation and HT at 1000°C for 10 min (IPF-Y and {100} pole figure in Figure 1(g,h)), revealing much finer grains and weaker texture along $<100>$ with significantly lower intensity of <5 MUD. Figure 1(i–l) quantitatively shows the distributions of grain sizes and aspect ratios in the as-SLM (Figure 1(i–j)) and SLM + HT (Figure 1(k,l)) Ti-5553, respectively. HT coarsened the grains from $\sim$10–40 µm (Figure 1(i)) to $\sim$50–200 µm with a few even larger (Figure 1(k)). It is also obvious that HT significantly reduced the aspect ratios from mostly >5 (up to 25) to $\sim$1–3, indicating morphological change form columnar to equiaxed.

Figure 2(a–c) shows SEM of the SLM Ti-5553 after HT at 1000°C for 30–120 s, revealing the early stages of the formation of the equiaxed grains. Thanks to homogenisation, most internal cells disappeared after 30 s, although there were still some in isolated areas (Figure 2(a)). The melt pool and layer boundaries were recognisable, but the etch pits in the boundaries (inset in Figure 2(a)) were not as clear as those before HT (Figure 1(d)). By counting the etch pits (selectively yellow arrowed), the dislocation density was estimated to be $\sim 10^6$–10^7 cm^{-2}, too low to cause recrystallisation. The number of dislocations decreased drastically after HT for 60–120 s (Figure 2(b,c)), indicating recovery. There was no recrystallisation even after 120 s which would be long enough for significant recrystallisation if there were enough dislocations [12]. Instead, longer HT caused first the melt pool and layer boundaries to become less well defined (after 60 s, Figure 2(b)), and ultimately their complete disappearance after 120 s (Figure 2(c)). The residual internal cells also vanished in both cases. The grain boundaries turned wavy after 60 s and serrated substantially after 120 s, creating thin necks in the β columns.

Dislocation configurations were investigated using TEM (Figure 3). Dislocations arrayed with spacing of <15 nm in the melt pool and layer boundaries (Figure 3(a,b)), confirming that the etch pits in Figure 1(d) are dislocations. A much smaller number of individual dislocations were found inside the grains and in grain boundaries (arrowed in Figure 3(c,d)). Since the formation of dislocations during SLM stems from thermal stresses [13], it is reasonable to assume that the Burgers vectors (b) are of $<111>$ type. In the particular example of Figure 3(d), BF TEM with the diffraction vector (g) of 002 makes all $<111>$ dislocations visible since $g \cdot b \neq 0$. Figure 3(e–g) shows TEM after HT at 1000°C for 60 s. Dislocation arrays in the melt pool boundaries became less dense with larger dislocation spacing of >30 nm (Figure 3(e,f)), indicating dislocation annihilation. This, together with compositional homogenisation, could explain the diffuse melt pool boundaries in Figure 2(b). The observations (Figure 2) that HT led to a significant reduction in the number of dislocations were supported by TEM at different tilting angles. For example, Figure 3(g) shows no dislocations although g is 011 and all $<111>$ dislocations, except for $[11\bar{1}]$and $[1\bar{1}1]$, should be visible.

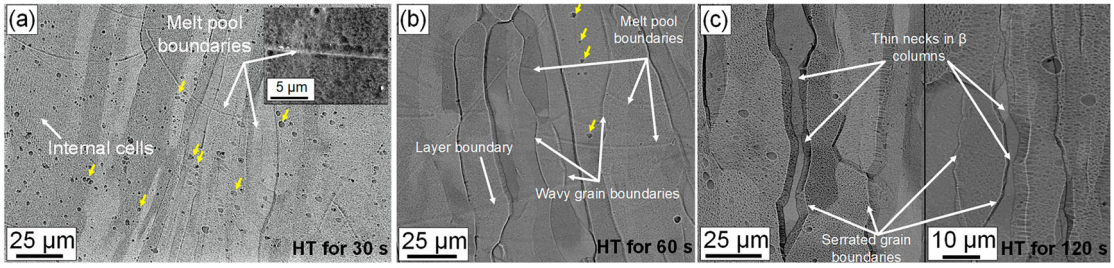

Figure 2. SEM of the SLM-fabricated Ti-5553 after HT at 1000°C for (a) 30 s, showing dislocation etch pits (selectively arrowed), melt pool boundaries, and some isolated internal cells, (b) 60 s, showing wavy grain boundaries and diffuse melt pool and layer boundaries, and (c) 120 s, revealing serrated grain boundaries creating thin necks in β columns.

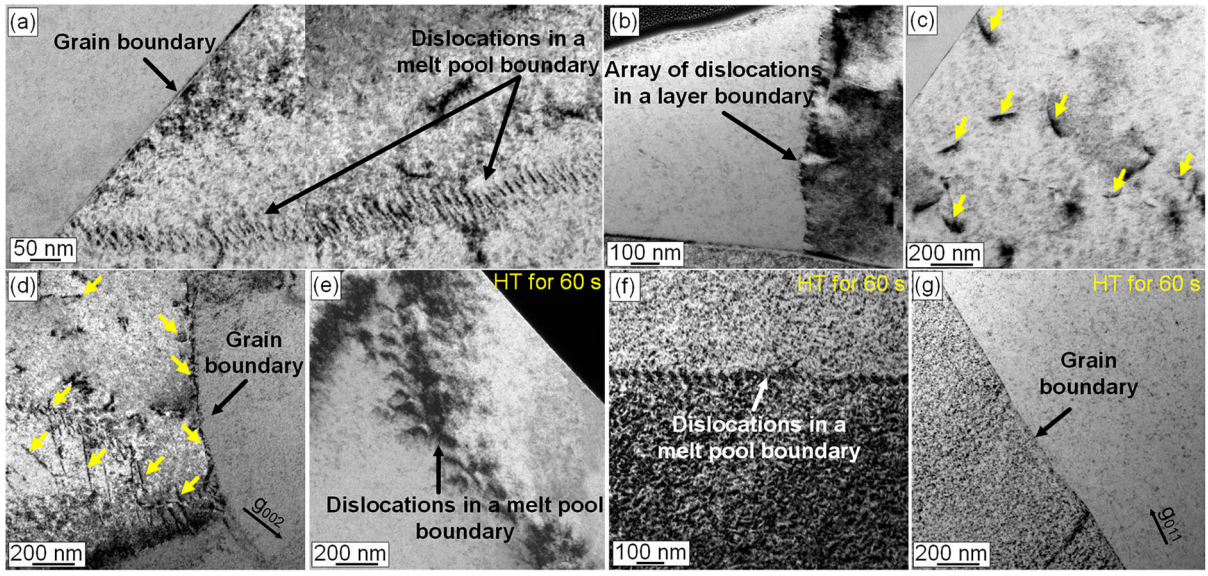

Figure 3. BF TEM of the as-SLM Ti-5553, showing arrays of dislocations in (a) a melt pool boundary and (b) a layer boundary, and individual dislocations (c,d) inside β grains and in grain boundaries (arrowed). BF TEM after HT at 1000°C for 60 s, showing (e,f) arrays of dislocations in melt pool boundaries and (g) absence of dislocations inside β grains and in grain boundaries.

4. Discussion

In contrast to the current knowledge, the results here suggest that neither martensitic α' decomposition [9] nor recrystallisation [8,9] is responsible for the formation of the equiaxed β grains after HT of the SLM Ti-5553. The former is not applicable since no martensite forms in Ti-5553 owing to high contents of β stabilising elements. Recrystallisation is also ruled out considering the dislocation configurations observed. Deformation-driven recrystallisation requires a high number of dislocations being entangled so that they do not undergo annihilation during HT [14]. Only individual dislocations are identified here which tend to disappear after HT at 1000°C (Figure 3). In fact, the dislocation density of $\sim 10^6$–10^7 cm^{-2} before HT (Figure 2(a)) is too low (at the lower end of 10^7–10^8 cm^{-2} for annealed metals [15] and well below that, i.e. $> 10^9$ cm^{-2} in cold worked metals, required for recrystallisation) and there is no recrystallisation even after longer times of HT (Figure 2(b,c)). Higher dislocation density in the arrays shown in Figure 3(a,b) is also incapable of initiating recrystallisation as dislocations annihilate during HT to produce larger spacing (Figure 3(e,f)), indicating recovery. This argument is reinforced by the unchanged texture after HT (Figure 1(f)). If recrystallisation were responsible for the formation of the equiaxed grains, their sizes would have been much smaller and orientations much more random, as in Figure 1(g,h) (SLM + tensile deformation + HT).

The formation of the equiaxed grains during HT, however, significantly reduces the grain boundary area (i.e. ρ_{GB} reduced by 8 times). SolidWorks was used to model the microstructure of the as-SLM alloy and that after HT for 10 min, as shown in Figure 4(a,b). The β columns are modelled as hexagonal prisms of ~ 400 µm long with base edge of < 40 µm based on Figure 1(a,i,j), while the equiaxed grains as Weaire-Phelan structures with the edge size of ~ 100 µm based on Figure 1(e,k,l). For a cube of ~ 7 mm used in the modelling, enough to include a large number of grains, the surface area of the columnar structure is calculated to be $> \sim 320$ mm^2, much larger than that of ~ 220 mm^2 of the equiaxed structure. Therefore, the morphological change can be explained using a combination of Plateau-Rayleigh instability and grain growth driven by the reduction in the surface area. Plateau-Rayleigh instability [16,17], often called Rayleigh instability, explains the breakup of rod-like (high-aspect-ratio) structures into spherical shapes. The initially smooth rod surface becomes wavy due to axial perturbations. Perturbations with $\lambda/D > \pi$, where λ is the wavelength and D rod diameter, are amplified owing to the local direction of the surface tension, leading eventually to the breakage [16,17]. Although Rayleigh instability was first used to explain the breakage in liquid jets (e.g. tap water) [18] and balling during laser deposition [19], it has been observed in solids, as in the examples of spheroidisation of lamellar structures at high temperatures in Al-10Si [20], steels [21,22] and TiAl/Ti_3Al [23].

Such mechanism appears to be operating during HT at 1000°C of the as-SLM Ti5553, as illustrated in Figure 4(c–e). At the early stage, thermal fluctuation of atoms, particularly solute ones, in grain boundaries

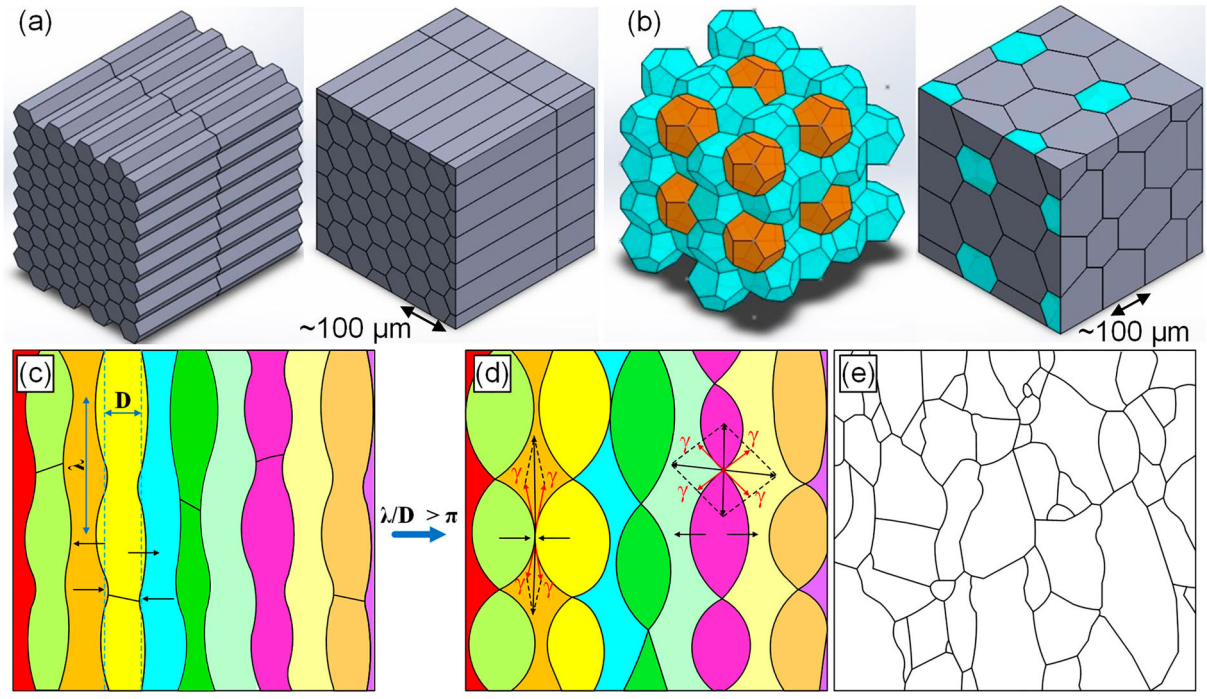

Figure 4. (a) Hexagonal prisms representing as-SLM β columns (left) in a cubic volume (right) and (b) Weaire-Phelan structure representing equiaxed β grains formed after HT (left) in the same cubic volume (right). (c–e) Model of the process leading to the morphological change from β columns to equiaxed grains, illustrating (c) formation of wavy boundaries (of bulging convex and pinching concave ones) as a result of boundary migration driven by forces from surface tension (black arrows) and (d) formation of grain boundary nodes where the concaved and convex sections meet, respectively, leading to redistribution of surface tension (γ) and creation of forces in different directions (black arrows), and this eventually produces the equiaxed grains in (e) after grain growth.

and absorption of dislocations into the boundaries lead to grain boundary roughening [24,25] and ultimately wavy shapes (Figures 2(b) and 4(c)). The Rayleigh instability criterion of $\lambda/D > \pi$ is fulfilled since $\lambda/D > 4$ (Figure 2). The surface tension (arrowed) forces the convex boundaries to bulge and the concave ones to shrink, creating thin necks and grain boundary nodes (Figures 2(b,c) and 4(d)). Additionally, inner grain boundaries in the columns can contribute to the formation of nodes through grain grooving [26]. In the case of balling, liquid jets, or spheroidisation of high-aspect-ratio lamellae, spherical particles are formed since the surrounding phase (e.g. air in falling water beads and ferrite in cementite spheroids) can fill the spacing between them. However, in SLM Ti-5553, spherical grains cannot form because there is no surrounding phase to fill the gap. Instead, the bulging and pinching sections would meet, respectively, to form nodes, causing redistribution of surface tension (γ) and forces in new directions (black arrows in Figure 4(d)). The balances between these forces would drive grain growth, eventually creating the equiaxed but coarsened grain structure shown in Figure 4(e) (observed in Figure 1(e)). The final grain size after HT at 1000°C for 10 min can be estimated using $D^n - D_0^n = Kt$, where t (s) is time and the constants n and K for Ti-5553 at 900°C (close to the temperature used here) are ~ 2 and 49 $\mu m^2/s$, respectively [12]. Taking $D_0 = \sim 40$ μm (the initial β columnar width, Figure 1(a)) results in $D = 176$ μm, in good agreement with the observation (Figure 1(k)). In conclusion, the equiaxed β grains form by the breakup of high-aspect-ratio β columns without nucleation of new crystals with different orientations, maintaining the general texture of the as-SLM alloy (Figure 1).

Such formation of equiaxed grains is similar to geometric dynamic recrystallisation (GDRX) in Al alloys during hot rolling [27]. Deformation elongates the grains, increasing their aspect ratios to >2–4. At the early stages, grain boundaries are serrated owing to the formation of subgrains. Further straining pinches off grain boundaries, breaking elongated grains into equiaxed ones. GDRX is geometrically equivalent to recrystallisation, but without nucleation and significant change in the existing texture. Comparing GDRX and the mechanism illustrated in Figure 4(c–e), the formation of the equiaxed grains during HT of SLM Ti-5553 can be considered as a deformation-free geometric recrystallisation. High-aspect-ratio grains are produced thanks to epitaxial growth (instead of rolling), grain boundaries are serrated by thermal fluctuations and moving of dislocations to the

boundaries (not subgrains), and finally, long grains are broken into equiaxed ones by surface tension (rather than external forces from rolling).

In summary, transformation of β columns to equiaxed grains during super-transus HT of SLM Ti-5553 was attributed to Rayleigh instability and grain growth driven by reduction in the grain boundary area. The equiaxed grains formed by breaking up the existing high-aspect-ratio columnar grains without nucleation and significant changes in orientation, similar to GDRX but with no deformation involved. This dismisses the belief that conventional recrystallisation is responsible, since the dislocation density was too low and the as-SLM texture was maintained after HT.

Acknowledgments

We are grateful to Ms. Alicia Harrison and Mr. Pedro Julio Orjuela Machuca for their contribution in producing Figs. 4a and b, and to Ms. Mogeng Li for useful discussion. We also appreciate the technical assistance and facilities provided by the Electron Microscopy Unit of Bio21 Institute at the University of Melbourne. The financial support by the Australian Research Council under DP190103557 is acknowledged.

Disclosure statement

No potential conflict of interest was reported by the authors.

ORCID

Ahmad Zafari http://orcid.org/0000-0003-4346-0675
Edward W. Lui http://orcid.org/0000-0002-0599-7749
Kenong Xia http://orcid.org/0000-0002-3469-435X

References

[1] Kou S. Welding metallurgy. Hoboken (NJ): Wiley; 2003.
[2] Vrancken B, Thijs L, Kruth JP, et al. Microstructure and mechanical properties of a novel β titanium metallic composite by selective laser melting. Acta Mater. 2014;68:150–158.
[3] Carroll B, Palmer T, Beese AM. Anisotropic tensile behavior of Ti–6Al–4V components fabricated with directed energy deposition additive manufacturing. Acta Mater. 2015;87:309–320.
[4] Wang F, Williams S, Colegrove P, et al. Microstructure and mechanical properties of wire and arc additive manufactured Ti-6Al-4V. Metall Mater Trans A. 2013;44:968–977.
[5] Chlebus E, Kuźnicka B, Kurzynowski T, et al. Microstructure and mechanical behaviour of Ti–6Al–7Nb alloy produced by selective laser melting. Mater Charact. 2011;62:488–495.
[6] Brandl E, Greitemeier D. Microstructure of additive layer manufactured Ti–6Al–4V after exceptional post heat treatments. Mater Lett. 2012;81:84–87.
[7] Yue H, Chen Y, Wang X, et al. Effect of beam current on microstructure, phase, grain characteristic and mechanical properties of Ti-47Al-2Cr-2Nb alloy fabricated by selective electron beam melting. J Alloys Compd. 2018;750:617–625.
[8] Wang J, Lin X, Li J, et al. Effects of deposition strategies on macro/microstructure and mechanical properties of wire and arc additive manufactured Ti 6Al 4V. Mater Sci Eng A. 2019;754:735–749.
[9] Nandwana P, Lee Y, Ranger C, et al. Post-processing to modify the α phase micro-texture and β phase grain morphology in Ti-6Al-4V fabricated by powder bed electron beam melting. Metall Mat Trans A. 2019;50:3429–3439.
[10] Fanning JC. Properties of TIMETAL 555 (Ti-5Al-5Mo-5V-3Cr-0.6Fe). J Mater Eng Perform. 2005;14:788–791.
[11] Jones N, Dashwood R, Dye D, et al. Thermomechanical processing of Ti–5Al–5Mo–5V–3Cr. Mater Sci Eng A. 2008;490:369–377.
[12] Zafari A, Ding Y, Cui J, et al. Achieving fine beta grain structure in a metastable beta titanium alloy through multiple forging-annealing cycles. Metall Mater Trans A. 2016;47:3633–3648.
[13] Murr LE. Metallurgy of additive manufacturing: examples from electron beam melting. Addit Manuf. 2015;5:40–53.
[14] Jourdan C, Gastaldi J, Grange GC. Nucleation of the titanium α and β phases. In situ study of the dislocation role by synchrotron X-ray topography. Phase Transit. 1989;14:201–208.
[15] Williamson GK, Smallman RE. Dislocation densities in some annealed and cold-worked metals from measurements on the X-ray debye-scherrer spectrum. Philos Mag. 1956;1:34–46.
[16] Rayleigh L. On the instability of jets. Proc London Math Soc. 1878;1:4–13.
[17] Chandrasekhar S. Hydrodynamic and hydromagnetic stability. Oxford: Clarendon Press; 1970.
[18] Lin SP, Reitz RD. Drop and spray formation from a liquid jet. Annu Rev Fluid Mech. 1998;30(1):85–105.
[19] Gibson I, Rosen DW, Stucker B. Additive manufacturing technologies: rapid prototyping to direct digital manufacturing. Boston (MA): Springer; 2010.
[20] Furuta S, Kobayashi M, Uesugi K, et al. Observation of morphology changes of fine eutectic Si phase in Al-10%Si cast alloy during heat treatment by synchrotron radiation nanotomography. Materials. 2018;11:1308.
[21] Payson P, Hodapp W, Leeder J. The spheroidizing of steel by isothermal transformation. Trans Am Soc Metals. 1940;28:306–332.
[22] Chattopadhyay S, Sellars CM. Kinetics of pearlite spheroidisation during static annealing and during hot deformation. Acta Metall. 1982;30:157–170.
[23] Bartholomeusz MF, Wert JA. The effect of thermal exposure on microstructural stability and creep resistance of a two-phase TiAl/Ti3Al lamellar alloy. Metall Mater Trans A. 1994;25:2371–2381.
[24] Yoon DY, Cho Y. Roughening transition of grain boundaries in metals and oxides. J Mater Sci. 2005;40:861–870.
[25] Han J, Thomas SL, Srolovitz DJ. Grain-boundary kinetics: A unified approach. Prog Mater Sci. 2018;98:386–476.
[26] Han F. Cellular automata modeling of Ostwald ripening and Rayleigh instability. Materials. 2018;11:1936.
[27] Konopleva E, McQueen H, Evangelista E. Serrated grain boundaries in hot-worked aluminum alloys at high strains. Mater Charact. 1995;34:251–264.